Title
Lithium-Sulfur Batteries with a Block Copolymer Electrolyte Analyzed by X-ray Microtomography

Journal
Journal of The Electrochemical Society, 167(6)

ISSN
0013-4651

Authors
Devaux, Didier
Villaluenga, Irune
Jiang, Xi
et al.

Publication Date
2020-01-04

DOI
10.1149/1945-7111/ab7c6c

Peer reviewed

Lithium-Sulfur Batteries with a Block Copolymer Electrolyte Analyzed by X-ray Microtomography

Didier Devaux,[1,2,3] Irune Villaluenga,[1,2,3] Xi Jiang,[4] Yu Hao Chang,[1,2,3] Dilworth Y. Parkinson,[5] and Nitash P. Balsara[1,2,3,4,z]

[1]*Energy Storage and Distributed Resources Division, Lawrence Berkeley National Laboratory, Berkeley, California 94720, United States of America*

[2]*Department of Materials Science and Engineering, University of California, Berkeley, California 94720, United States of America*

[3]*Joint Center for Energy Storage Research (JCESR), Lawrence Berkeley National Laboratory, Berkeley, California 94720, United States of America*

[4]*Materials Sciences Division, Lawrence Berkeley National Laboratory, Berkeley, California 94720, United States of America*

[5]*Advanced Light Source Division, Lawrence Berkeley National Laboratory, Berkeley, California 94720, United States of America*

Most of the work on Lithium-sulfur (LiS) batteries use liquid electrolytes that have limited stability when coupled with Li metal anodes. We have studied LiS batteries with a solid block copolymer electrolyte which exhibits improved stability against Li anodes. The electrolyte comprises a polystyrene-*b*-poly(ethylene oxide) (SEO) copolymer doped with a Li salt. Hollow carbon nanospheres impregnated with sulfur were used to build a composite cathode. Two types of sulfur-impregnated functionalized carbon nanospheres were used: one with carboxylic acid groups and the other with short lithium poly(4-styrenesulfonyl (trifluoromethylsulfonyl)imide) (PSTFSI-Li) chains. Cells with Li_2S_8 dissolved in the SEO based electrolyte served as the baseline. After cycling, the reason for capacity fade was determined by imaging the batteries using synchrotron hard X-ray microtomography. It is generally assumed that LiS cells fail due to dissolution of polysulfide into the liquid electrolyte, i.e., the main problems related to the cathode. In our all-solid cells, failure was primarily due to delamination of the Li foil from the polymer electrolyte layer. Delamination is also observed at the sulfur cathode. It is likely that the large changes in volume of the active materials during cycling induce delamination in all-solid LiS cells.

The development of electrochemical energy storage devices is fostered by the seemingly never-ending demands of higher energy density and improved safety.[1] Lithium-ion batteries are dominant today for many applications, from small electronic devices up to hybrid and fully electric vehicles.[2] Despite a relatively low operating voltage of about 2.15 V, sulfur (S_8) is an attractive cathode for rechargeable batteries due to its high theoretical specific capacity of 1672 $mAh.g^{-1}$, a factor of six higher than more traditional cathodes (274 $mAh.g^{-1}$ theoretically for $LiCoO_2$).[3] In addition, S_8 is a non-toxic, low cost, and naturally abundant. In order to realize high energy density systems, the S_8 cathode must be paired with a Li metal anode. The theoretical energy density of a lithium-sulfur battery is 2547 $Wh.kg^{-1}$ while that of a graphite-sulfur battery is 576 $Wh.kg^{-1}$; graphite is the anode in lithium-ion batteries.[4]

Many challenges remain to be addressed to effectively couple a negative Li metal electrode with a positive S_8 electrode. An intrinsic problem with this chemistry is the large volume change between charged and discharged states.[5,6] Additional problems arise due to the low S_8 utilization, poor capacity retention, limited cycle life, and low coulombic efficiency.[7] During the initial discharge, S_8 is reduced to chain-like Li polysulfides intermediates of different sizes and ultimately to Li sulfide. Some of the polysulfides are soluble in the electrolytic phase, and they migrate to the Li anode where they are oxidized. This is the start of a redox shuttle wherein electrons are consumed as reduced and oxidized polysulfides diffuse and migrate between the two electrodes, resulting in a loss of active material—it is generally assumed that this is the reason for the observed capacity fade and coulombic efficiency decay.[8] Moreover, S_8 and the final product Li_2S are electronic and ionic insulators, and this limits cathode utilization to regions in close proximity to the electronically conducting particles. Self-discharge of partially discharged LiS batteries due to the polysulfide shuttle is yet another problem.[9]

Confining the sulfur within mesoporous and nanoporous carbon is one approach to address the polysulfide dissolution problem.[10–15] By confining S_8 in carbon nanospheres, cells containing a liquid electrolyte and Li metal anodes exhibit 90% capacity retention after 100 cycles.[16] Liquid electrolytes are, however, not stable against Li metal anodes.[17] Solid block copolymer electrolytes with a rigid non-conducting block and a flexible conducting block are promising candidates for stabilizing lithium metal anodes.[18–21] In this work we study cells made of a lithium metal anode, a cathode comprising sulfur-impregnated carbon nanospheres, and a block copolymer electrolyte. The cells were cycled and as one might expect, they exhibited significant capacity fade. We also use hard X-ray microtomography to determine the reason for the capacity fade. Our observations indicate that polysulfide dissolution was not the primary reason for cell failure in our system.

Experimental

Hollow carbon nanospheres were synthesized using the approach of Hee et al.[16] A 1 ml aqueous solution of ammonia (28 wt%) was added to 26.6 ml of deionized water and ethanol (1:7 vol:vol) and stirred for 30 min at room temperature. Tetraethyl orthosilicate (0.93 ml), resorcinol (0.13 g), and formalin (37 wt%, 0.19 ml) were added to the solution in two steps with a waiting time between steps of about 10 min. The resulting mixture was stirred at room temperature for 24 h and heated at 100 °C for 24 h in a Teflon autoclave. The product was collected by centrifugation and dried in an oven. The oven temperature was ramped up at a rate of 5 $°C.min^{-1}$ up to 750 °C and maintained at that temperature for 1 h. The oven was continuously flushed with argon. The final product, a black solid comprising spherical particles with silica cores and carbon shells, was collected and suspended by stirring in a 15 wt% HF aqueous solution for 2 d. This results in the dissolution of the silica cores. The hollow carbon nanospheres were then dissolved in nitric acid at 80 °C for 2 h in order to functionalize

[z]E-mail: nbalsara@berkeley.edu

the surface of the carbon nanosphere with carboxylic acid (COOH) groups. The functionalized spheres were isolated by centrifugation and washed with distilled water until the pH of the water was neutral. The functionalized carbon nanospheres were dried under vacuum at 90 °C for 3 d.

The hollow carbon nanospheres thus obtained were examined by Scanning Transmission Electron Microscopy (STEM). A dilute aqueous solution of carbon nanospheres was drop cast and dried on a lacey carbon coated copper grid (Electron Microscopy Sciences). The grid was examined using a Tecnai F20 UT FEG equipped with a high angle annular dark field (HAADF) detector. The acceleration voltage was 200 keV.

The carbon nanospheres were impregnated with S_8 (Alpha Aesar) by dry mixing at 155 °C for 12 h in a oven. The carbon-to-sulfur ratio was changed to systematically vary the composition of the impregnated spheres. Thermogravimetric analysis (TGA) was used to determine the composition of the impregnated spheres. The samples were heated to 600 °C at 10 °C.min^{-1} under argon, and the ratio of the initial and final weights were used to determine the composition, assuming that all of the sulfur was evaporated at the end of the TGA scan.[22] Three compositions were used: $w = 0.3$, 0.5, or 0.6 where the number reflects the weight fraction of sulfur within the carbon nanospheres. These materials are denoted $S_8(w = x)$/C with $x = 0.3$, 0.5, or 0.6.

The surfaces of some of the COOH-functionalized sulfur-containing nanospheres were subjected to an additional reaction step. First, (N-(2-methylpropyl)-N-(1-diethylphosphono-2,2-dimethylpropyl)-O-(2-carboxyprop-2-yl)hydroxylamine) (MAMA-SG1) macroinitiator based on alkoxyamines was functionalized with 2-hydroxyethylacrylate under the conditions described in Ref. 23. 4-styrenesulfonyl(trifluoromethyl-sulfonyl)imide potassium (SKTFSI) monomer was polymerized using functionalized MAMA-SG1 with OH groups as initiator in dimethylformamide at 115 °C, followed by the exchange of the cations K^+ to Li^+ by dialysis using a solution of lithium chloride to yield functionalized PSLiTFSI with OH groups. The molecular weight of functionalized PSLiTFSI was 2500 g.mol^{-1}. This was determined using inductively coupled plasma optical emission spectrometry (ICP-OES) and liquid ^{1}H NMR Finally, the polymer was added at a 0.51 weight fraction to a suspension of carbon-sulfur nanospheres functionalized with COOH groups in acetone. The suspension was stirred at 58 °C for 3 h in order to attach PSLiTFSI functionalized with OH groups to the surface of carbon-sulfur nanospheres with COOH groups. The suspension was centrifuged to remove the unreacted PSTFSI-Li. This material is denoted $S_8(w = 0.6)$/C-PSTFSI.

A field emission scanning electron microscope (SEM, JSM-7500F, JEOL) was used to image the sulfur-impregnated carbon nanospheres. The composition of the nanospheres was analyzed using a built-in energy-dispersive spectrometry (EDS) X-ray detector (Thermo Scientific).

The polystyrene-b-poly(ethylene oxide) (SEO) block copolymer was synthesized by sequential anionic polymerization as described previously.[18,19] The averaged molecular weights of polystyrene and poly(ethylene oxide) are 380 and 300 kg.mol^{-1}, respectively, with an overall dispersity index of 1.23. Inside the antechamber of an argon filled glove box the SEO block copolymer was dried under vacuum at 90 °C for 24 h and the lithium bis (trifluoromethanesulfonyl)imide (LiTFSI) from Novolyte was dried at 120 °C for 3 d. Inside the glove box, the SEO and LiTFSI was dissolved in N-methyl-2-pyrrolidone (NMP, EMD Millipore) and mixed at 90 °C for 12 h. The molar ratio r of Li^+ to ethylene oxide moieties in the polymer electrolyte is fixed at 0.085.[24] The solution was then cast on a nickel (Ni) foil (All Foils, Inc.) using a doctor blade and a home-built casting device. An electrolyte film was obtained by letting the solution dry at 65 °C for 12 h. A resulting membrane with average thickness of 34.2 ± 8.4 μm is peeled off from the Ni foil and subsequently dried in the glove box ante-chamber under vacuum at 90 °C for 12 h.

To prepare the composite cathode, a solution of SEO/LiTFSI at $r = 0.085$ in NMP was prepared by stirring at 90 °C for 12 h. Carbon black (Denka) and sulfur-impregnated carbon nanospheres were added to the solution. The resulting slurry was then thoroughly mixed in a homogenizer (Kinematica) at 5,000 rpm for several minutes and cast on a 20 μm thick electrochemical grade aluminum (Al) foil using a doctor blade on the home-built casting unit. The electrode was dried at 60 °C for 12 h in the glove box and for an additional 12 h at 50 °C in the glove box antechamber. The electrode foil was then stored in the glove box for at least a week prior use. The different cathode formulations used in this study are listed in Table I. A typical formulation comprises 13.1 wt% sulfur-impregnated carbon nanospheres, 56.5 wt% SEO/LiTFSI, and 30.4 wt% carbon. The S_8 loading, estimated using the mass of cathode disk replicates and the measured value of w, is also provided in Table I. A cathode made of 13 wt% Li_2S_8, 56.7 wt% SEO/LiTFSI, and 30.3 wt % carbon was also made to serve as a baseline.[25] The Li_2S_8 was obtained inside the glove box by mixing of the appropriate ratio of elemental S_8 and Li_2S in a NMP at 90 °C for 12 h.[26,27] This solution was then mixed with SEO/LiTFSI and carbon and cast onto an Al foil.

All the batteries were assembled inside an Argon glove box. A 1.1 cm diameter positive electrode disk was punched out and pressed onto a 1.43 cm diameter SEO/LiTFSI disk. Then, a 1.27 cm diameter Li disk was pressed onto the SEO electrolyte film. Al and Ni tabs were taped on the cathode and anode, respectively. The battery assembly was placed in an Al-laminated pouch bag (Showa Denko) and vacuum sealed (Packaging Aids Corp). For each positive active material, five to six battery replicates were assembled. Average values and standard deviation (represented by error bars in the figures) of parameters reported here were calculated from these replicates. The batteries are thus denoted Li-$S_8(w = x)$/C, Li-$S_8(w = 0.6)$/C-PSTFSI, and Li-Li_2S_8 when the cathodes contain $S_8(w = x)$/C, $S_8(w = 0.6)$/C-PSTFSI and Li_2S_8, respectively.

After their assembly, the batteries were transferred inside a 90 °C oven, connected to a Maccor battery cycler, and annealed for 12 h prior cycling without the application of controlled pressure (the external pressure in our experiments was about one atmosphere). The cycling rate is reported in term of C/n where n is the number of hours used to charge or discharge the battery. The cycling procedure comprises an initial discharge at a low current density corresponding to C/30, followed by 100 cycles at a higher current density, both in charge and discharge, and corresponding to C/12. The current density applied for each C-rate was calculated based on the S_8 loading within each cathode (see Table I) and the electrode diameter. All the reported potential (E) in the text are given relatively to the

Table I. Positive electrode formulation comprising carbon nanospheres impregnated with sulfur. The sulfur loading is an average based on the positive electrode disk replicates.

Active Material	Active Material (wt%)	SEO/LiTFSI (wt%)	Carbon (wt%)	S_8 loading (mg.cm^{-2})
$S_8(w = 0.3)$/C	13.8	55.9	30.3	0.09 ± 0.01
$S_8(w = 0.5)$/C	13.9	56.0	30.1	0.13 ± 0.02
$S_8(w = 0.6)$/C	12.9	56.6	30.5	0.14 ± 0.01
$S_8(w = 0.6)$/C-PSTFSI	11.7	57.4	30.9	0.14 ± 0.01
Li_2S_8	13.0	56.7	30.3	0.30 ± 0.04

Li^+/Li^0 couple. Galvanostatic (constant current) charge and discharge steps were performed between 1.5 and 3 V with 45 min rest period in between. For each cycle (N) the capacity (Q) during the charge step (Q_c) and discharge step (Q_d) are calculated by integrating the current over time and normalized by the estimated mass of S_8 in the cathode, using the measured mass of each electrode disk and assuming a constant composition. The Coulombic efficiency (η) is defined as the ratio between Q_d and Q_c at each cycle N when $N \geqslant 1$. $N = 0$ corresponds to the initial $C/30$ discharge.

After cycling, some of the batteries were returned to the glove box for disassembly. The electrodes were gently separated and a portion of the cathode was cut. These electrode pieces were transferred to the SEM apparatus using a desiccator and a glove bag filled with Argon to minimize air exposure. The surface of the S_8 electrode that faced the polymer electrolyte separator was imaged at a beam current of 20 μA and an accelerating voltage of 5 kV. Similarly, portions of S_8 electrode prior battery assembly were also imaged. Some of the batteries were also characterized by hard X-ray microtomography prior to and after cycling. The tomography samples were prepared according to a previous methodology.[28,29] The pouch bag of the batteries were opened in the glove box and a 3.175 mm diameter punch was used to cut out small battery portions which were sealed again in a pouch bag. The same procedure was used to prepare samples of uncycled batteries that were heated at 90 °C for 12 h. The repouched small battery samples were transferred to the hard X-ray microtomography beamline 8.3.2 at the Advanced Light Source.[30] There, monochromatic synchrotron hard X-rays of 25 keV energy were used to illuminate the samples at room temperature during a 180° rotation. The transmitted X-rays were first converted into visible light using a 20 μm thick LuAG scintillator. Then, the light was converted into digital image file thanks to an optical microscope with a 10x lens equipped with a sCMOS camera leading to square pixels of 0.64 μm. After processing, the radiograph images were stacked together to obtain a 3D volume that was analyzed by the Avizo software.

Results and Discussion

Prior sulfur impregnation, the synthesized carbon particles with carboxylic acid groups were characterized by STEM. Figure 1a shows a representative image with a magnified version in the inset. The carbon materials have a well-defined spherical hollow morphology similar to that reported by He et al.[16] On average the carbon nanospheres have an outer diameter of 202 ± 7 nm and a wall thickness of 13.1 ± 0.4 nm. The nanosphere walls are porous; BET analysis revealed that pore sizes range from 1 to 1.3 nm.[22] After sulfur impregnation, SEM and EDS was performed. Figure 1b shows a typical SEM image of the $S_8(w = 0.6)$/C materials with a magnified image in the inset. The morphology of the carbon-sulfur nanospheres is preserved after sulfur impregnation. From the SEM image, it can be deduced that the average diameter of the impregnated spheres is 221 ± 4 nm. SEM was also performed on the $S_8(w = 0.3)$/C and $S_8(w = 0.5)$/C particles and their diameters lie within the standard deviation of the $S_8(w = 0.6)$/C average diameter. The impregnation of sulfur within the hollow carbon sphere leads to an estimated volume increase of about 32%. It has not been possible to determine if this volume increase is due to an increase in the inner or outer diameters (or perhaps both). In addition, some cracked nanospheres are observed after impregnation. This result was seen for all the compositions of sulfur within the carbon nanospheres.

Before battery cycling, the cathodes were characterized by SEM. A typical image of the $S_8(w = 0.6)$/C based electrode prior cycling is shown in Fig. 2a. The composite electrode shows two distinct portions. One with a homogeneous distribution of active material in shape of well-defined spheres and carbon black embedded in the polymer electrolyte. The other part is made mainly of spheres agglomerates. These agglomerate regions arise from the non-homogeneous dispersion of materials within the slurry during cathode processing. The cathode is highly porous (porosity > 50%) due to the casting process used. In addition, to preserve the structure of the carbon-sulfur nanospheres, hot pressing was not performed on the electrode after their formulation.[31] Similar texture and electrode morphology were observed by SEM for the cathode comprising $S_8(w = 0.3)$/C, $S_8(w = 0.5)$/C, and $S_8(w = 0.6)$/C-PSTFSI. On average, the typical diameter of the carbon-sulfur nanospheres in the electrodes are 221.9 ± 9.0 nm, independent of the sulfur content or surface functionalization. This diameter is close to the one measured prior electrode formulation. The electrode formulation process has no discernible impact on the morphology of the carbon-sulfur nanospheres. However, a few carbon-sulfur nanospheres are defective, some are broken while others cracks as exemplified in the inset of Fig. 2a. After battery cycling, some batteries were opened in the glove box and portions of the cathode were recovered. A typical SEM image of cycled cathodes is given in Fig. 2b, corresponding to a post-cycled Li-$S_8(w = 0.6)$/C battery with a magnified view in the inset. The image of the cycled cathode is comparable to that obtained before cycling with a presence a similar proportion of defective nanospheres. The SEM images of cathodes from post-cycled batteries comprising $S_8(w = 0.3)$/C, $S_8(w = 0.5)$/C, and $S_8(w = 0.6)$/C-PSTFSI materials are similar to Fig. 2b. In addition, the diameter of the carbon-sulfur nanospheres after cycling are independent of the sulfur content or surface functional groups, with an average value of 225.7 ± 10.1 nm. This value lies in the error bars of the carbon-sulfur nanospheres diameter prior cycling. Generally

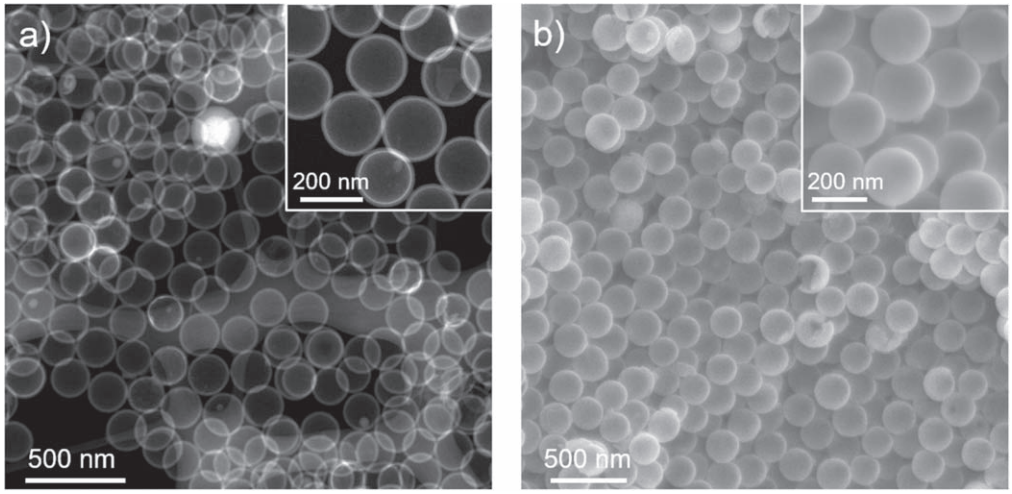

Figure 1. (a) STEM image of the hollow carbon nanospheres and (b) SEM image of the $S_8(w = 0.6)/C$ materials. For both images, the inset is a magnified picture.

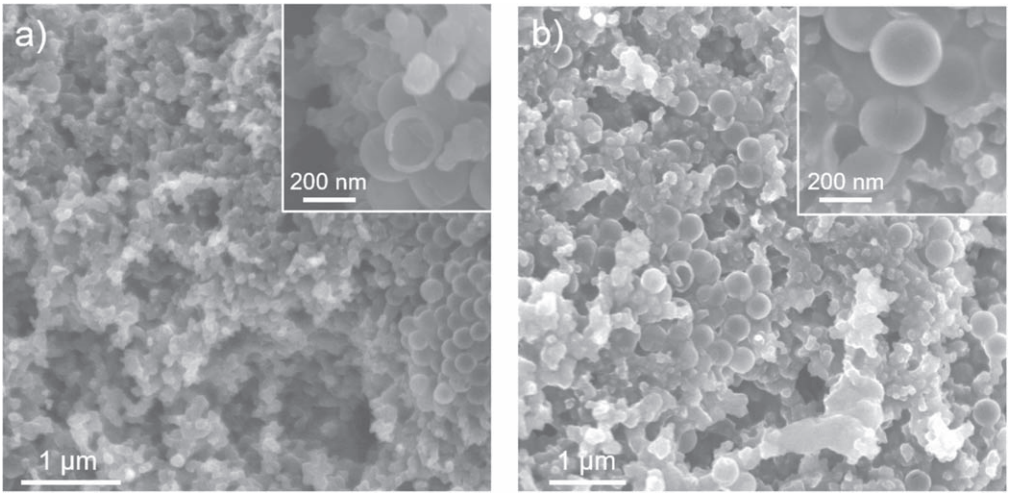

Figure 2. SEM images of the positive electrode comprising $S_8(w = 0.6)$/C active materials. (a) before and (b) after battery cycling.

cycling S_8 cathodes is expected to lead to morphological changes due to the dissolution of polysulfide intermediates. The lack of difference between Figs. 2a and 2b is thus surprising.

Li metal SEO based batteries were cycled at constant current. Figure 3 shows the cycling potential, E, as a function of the specific capacity Q for a typical battery comprising $S_8(w = 0.6)$/C as cathode active material during both charge or discharge steps. For clarity, only the initial discharge curve and the subsequent the cycling curves recorded every 10 cycles are presented up to 100 cycles. During the initial discharge at low current density the specific discharge capacity Q_d is 1088.7 mAh.g^{-1} which is a factor 1.54 lower than the theoretical S_8 capacity of 1672 mAh.g^{-1}. It is evident that only 66% of the sulfur atoms in our solid electrodes are redox-active. It is likely that the capacity of the electrodes may be improved by optimizing processing conditions. The main aim of this work is to determine the failure modes in the nanosphere-based electrodes with a solid polymer electrolyte; the limited efficacy of the electrodes used do not interfere with this aim. During the initial discharge at low current (C/30 rate), two plateaus are observed one at about 2.4 V which is generally ascribed to the lithium polysulfide reduction reaction and the second at 2.0 V corresponding to the formation of the insoluble Li_2S_2 and Li_2S compounds.[32,33] During this initial discharge step, the capacity corresponding to the first and second plateaus represents 32% and 68% of the total discharge capacity, respectively. These values are consistent with literature data on sulfur batteries.[33,34] Then, after this discharge, the battery was subjected to a repeatedly cycling at a fixed higher current (C/12 rate) to monitor capacity retention over times. During the first charge, only 98.8% of the initial discharge capacity is recovered, and Q_c and Q_d decay with the cycle number N down to 339.6 and 294.6 mAh.g^{-1} at $N = 100$, respectively. For the Li-$S_8(w = 0.3)$/C, Li-$S_8(w = 0.5)$/C, Li-$S_8(w = 0.6)$/C-PSTFSI and Li-Li_2S_8 batteries the cycling behavior of E as a function of Q is similar to that observed for the Li-$S_8(w = 0.6)$/C batteries (Fig. 3).

Figure 4 displays the average values of Q_c and Q_d as a function of N for the Li-$S_8(w = 0.6)$/C and the reference Li-Li_2S_8 batteries. In addition, the η values calculated from the averaged capacities at each cycle is also presented on the secondary Y-axis. The two battery systems present a continuous decrease of Q_c and Q_d with N. For $N \geqslant 1$, the behavior is analogous for both battery systems with discharge capacities decaying by 1.03 ± 0.34 and 1.11 ± 0.63 mAh.g^{-1}.cycle^{-1} for the Li-$S_8(w = 0.6)$/C and Li-Li_2S_8 batteries, respectively. In addition, the discharge capacity is on average higher by a factor 2 for the Li-$S_8(w = 0.6)$/C battery than the Li-Li_2S_8 batteries. The impregnation of sulfur within a nanostructured carbon matrix enhances battery performance and cycle life, relative to the reference cell.

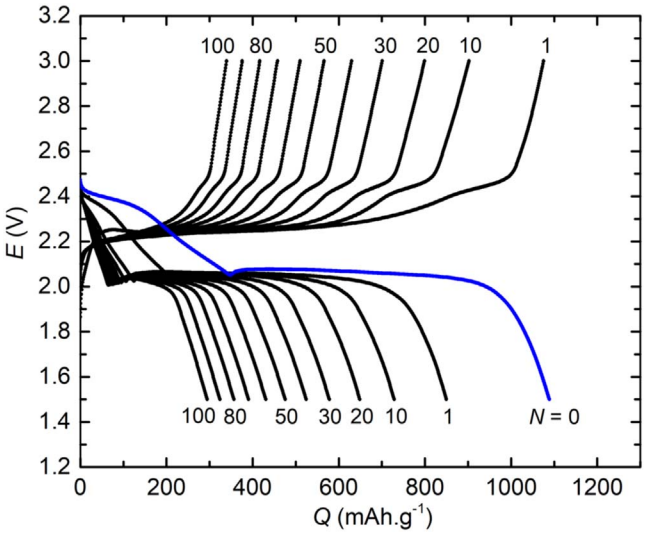

Figure 3. Potential E as a function of the specific capacity Q for a typical Li-$S_8(w = 0.6)$/C battery. The cycle numbers N are also indicated and $N = 0$ is the initial discharge step.

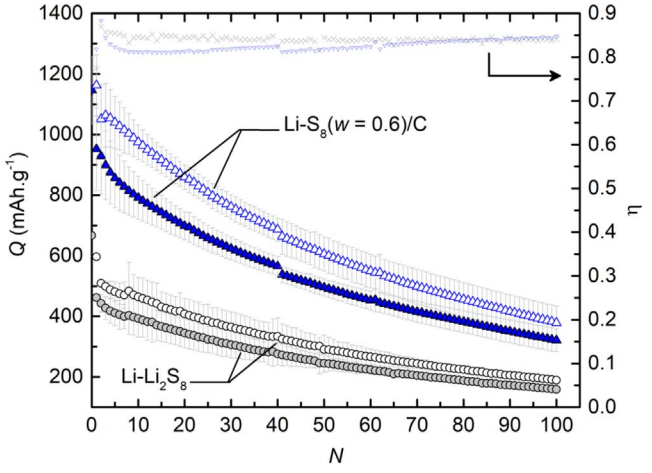

Figure 4. Average specific capacities Q in (open symbols) charge and (filled symbols) discharge as a function of cycle number N for the (triangle) Li-$S_8(w = 0.6)$/C and (circle) Li-Li_2S_8 batteries. The corresponding Coulombic efficiency (η) is given on the right axis for (▼) Li-$S_8(w=0.6)$/C and (×) Li-Li_2S_8 batteries.

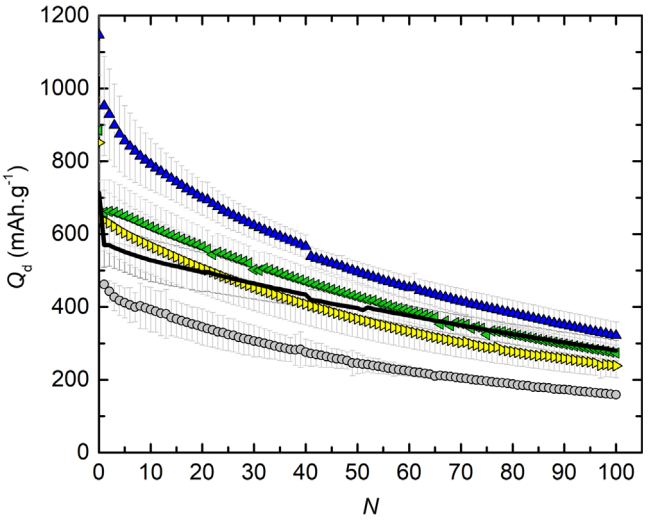

Figure 5. Average specific discharge capacities Q_d as a function of cycle number N for the (▷) Li-S_8($w = 0.3$)/C, (◁) Li-S_8($w = 0.5$)/C, (▲) Li-S_8($w = 0.6$)/C, (-) Li-S_8(w=0.6)/C-PSTFSI, and (●) Li-Li_2S_8 batteries.

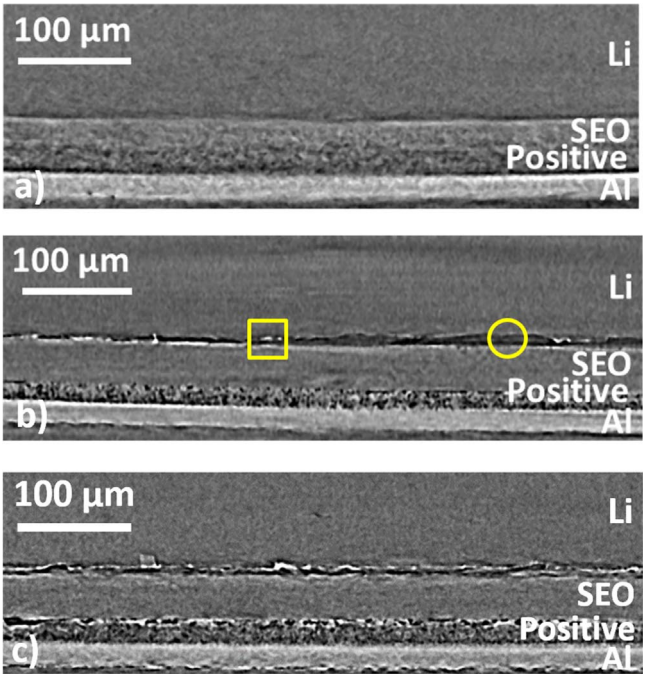

Figure 6. X-ray microtomography cross-sections of (a) uncycled Li-S_8($w = 0.6$)/C, (b) cycled Li-S_8($w = 0.6$)/C, and (c) Li-Li_2S_8 battery. The square and the circle show area of Li_2S deposits and Li/SEO delamination, respectively.

Figure 5 displays the N-dependence of Q_d for all of the different types of cells covered in this study: Li-S_8($w = x$)/C with $0.3 \leqslant x \leqslant 0.6$, Li-$S_8$($w = 0.6$)/C-PSTFSI, and the reference system, Li-Li_2S_8. Similar trends of Q_d versus N is observed for all cells. The discharge capacities decay for the batteries comprising Li-S_8($w = 0.3$)/C and Li-S_8($w = 0.5$)/C are 1.02 ± 0.25 and 1.05 ± 0.64 mAh.g^{-1}.cycle^{-1}, respectively. For the Li-S_8($w = 0.6$)/C-PSTFSI batteries, Q_d decays with N at 0.72 ± 0.17 mAh.g^{-1}.cycle^{-1}. The functionalization of the carbon nanospheres with PSTFSILi thus improves cell cyclability.

To identify the reason for the capacity fade reported in Fig. 5, some of the batteries were imaged by hard X-ray microtomography. All batteries were stopped either in the charge or discharge state after cycle $N = 100$. Figure 6 shows typical microtomography cross-sections of batteries obtained at room temperature. Figure 6a is an image of an uncycled Li-S_8($w = 0.6$)/C battery that was heated at 90 °C for 12 h prior obtaining the tomogram. Four distinct layers are seen in intimate contact with each other: Li, SEO, positive electrode, and Al current collector. The grayscale pixel values at that specific position in Fig. 6a corresponds to the relative X-ray absorption coefficient of the material at that location. Brighter pixels correspond to higher X-ray absorption at that position. The Al current collector appears brightest as it has the highest X-ray absorption coefficient. This is followed by the sulfur electrode that is adhered to the SEO separator. The other side of the SEO separator is in contact with the Li electrode. Only a portion of the 150 μm thick Li metal is shown as we are mainly interested in the active portion of the cell. The Li/SEO interface is embellished by a thin dark band on the negative electrode side and a thin bright band on the SEO side. This feature is typical of Fresnel phase contrast originated from samples containing interfaces.[28,29] The image shown in Fig. 6a is representative of all of the uncycled batteries containing the active materials listed in Table I.

Typical tomography slices of batteries stopped in discharged state after cycling comprising a S_8($w = 0.6$)/C cathode is shown in Fig. 6b. A broad non-uniform dark band is seen at the Li/SEO interface; this band is not seen in the uncycled cell (Fig. 6a). There are two main differences between this dark band and the dark Fresnel fringe in Fig. 6a: the dark band obtained after cycling is much darker and wider than the Fresnel fringe. The thickness of the dark band in Fig. 6b identified at one location by the circle is 9.4 ± 1.1 μm, which is much larger than the thickness of the Fresnel fringe in Fig. 6a (about 3 μm). The broad dark band in the cycled cell in Fig. 6b indicates the presence of a material with extremely low electron density, which we take to be air. In other words, the dark band in the cycled cell in Fig. 6b indicates delamination at the Li/SEO interface.[29,35] Following the procedure given in Ref.,[25] we determined the void fraction at this interface to be 0.75 ± 0.07. It is evident that delamination and the concomitant increase in current at the Li/SEO interface that does not contain voids must play a role in the observed capacity fade. This loss of contact may be mitigated by the application of controlled pressure (the external pressure in our experiments was about one atmosphere). In addition to the dark band representing voids, we find the presence of bright deposits in the vicinity of the Li metal electrode, shown for example in the square in Fig. 6b. These deposits are much brighter than all other features in Fig. 6b. We attribute these features to Li_2S deposits (or perhaps some other sulfur-containing electron-dense material). The theoretical linear X-ray absorption coefficient of Li_2S is about two times higher than that of Li metal at 25 keV.[36] This is qualitatively consistent with our observations. For concreteness, we refer to the bright features in the X-ray tomographs as Li_2S deposits. One expects to form Li_2S if the chemical reaction between the diffusing polysulfides species and Li metal goes to completion. In many cases, the voids at the Li/SEO interface lie above the Li_2S deposits. This suggests that the Li_2S deposits may have caused the delamination as they are insulating and impermeable to Li^+, and thus prevent redox reactions with the Li atoms that are above the deposits. The main difference between the uncycled and cycled cathodes in Figs. 6a and 6b are the presence of dark voids and bright Li_2S deposits throughout the cathode. While some voids are present in the as-cast cathode in Fig. 6a there are many more voids in the cycled cathode. Comparable dark (voids) and bright (Li_2S_2 deposits) features are observed at the Li/SEO interface on all the Li-S_8($w = x$)/C with $x = 0.3$, 0.5, and 0.6, and Li-S_8($w = 0.6$)/C-PSTFSI batteries irrespective of the state of the battery (charged versus discharged). For completeness, Fig. S1 is (available online at stacks.iop.org/JES/167/060506/mmedia) shows representative microtomography cross-sections of Li-S_8($w = 0.3$)/C, Li-S_8($w = 0.5$)/C, and Li-S_8($w = 0.6$)/C-PSTFSI batteries stopped in discharged state. In Fig. 6c we show tomography data from a typical cycled reference Li-Li_2S_8 battery. The main features seen in Fig. 6c are similar to those seen in Fig. 6b except for the fact that there are many more Li_2S deposits near the Li electrode in the reference battery. This indicates that the use of carbon to confine sulfur results in a decrease

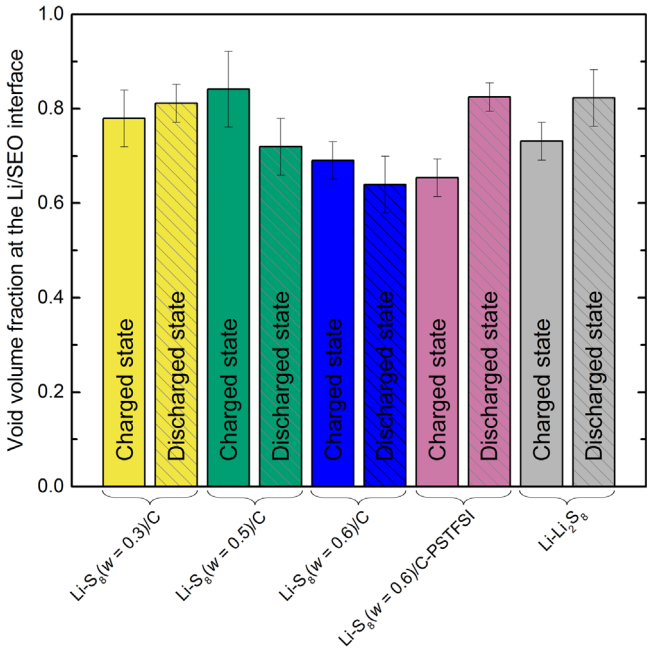

Figure 7. Void volume fraction at the Li/SEO interfaces.

in the side-reaction products. Our attempts to quantify the locations of the Li_2S deposits and voids in the cathode were unsuccessful due to interference from Fresnel fringes. Moreover, in Fig. 6c bright deposits on top of the cathode are also observed with linear X-ray absorption coefficient close to that found on the Li_2S deposits located on the anode side. In literature, the insulating Li_2S and S_8 materials are known to precipitate at electrolyte/cathode interface.[37] These bright features can then attributed to Li_2S and S_8 and are widely present in the reference cycled Li-Li_2S_8 battery compared to the cycled batteries comprising carbon-sulfur nanospheres (Fig. 6b and Fig. S1). In addition, most of these bright deposits are located underneath dark features, similar to the voids at the Li/SEO interface, at the interface between the cathode and the SEO electrolyte. It seems that delamination at the cathode/SEO interface can be provoked by the deposition of insulating redox products. The formation and evolution of this new dark feature remains to be investigated.

In Fig. 7, we summarize the results of our X-ray tomography at the Li/SEO interface. There is little difference between the reference cells and cells wherein the sulfur is confined within carbon nanospheres—sever delamination that accounts for about 75% of the electrode-electrolyte interface is seen in all cases.

Conclusions

We report on the cycling of all-solid batteries comprising a Li metal anode and a composite cathode wherein elemental sulfur is infused into functionalized carbon nanospheres. A film of a nanostructured polystyrene-*b*-poly(ethylene oxide) (SEO) block copolymer doped with a Li salt is used as battery separator. The same polymer/salt system is mixed into the composite sulfur cathode for providing ion-transporting pathways to the active particles. The capacity fade in these batteries was found to be similar regardless of sulfur content and functionalization. Synchrotron hard X-ray microtomography was used to determine the cause of capacity fade. Unlike most previous studies wherein problems are found within the sulfur cathode, we found that the main reason for capacity fade was due to changes near the electrolyte anode interface. We found the presence of voids and sulfur-containing solids (probably Li_2S) at this interface. It appears that the capacity fade in Li-S batteries is due to the loss of ionic contact between the solid block copolymer electrolyte and the lithium metal anode. This loss of contact may be mitigated by the application of controlled pressure (the external pressure in our experiments was about one atmosphere). We hope to examine the effect of pressure in future studies.

Acknowledgments

This work was supported by the Assistant Secretary for Energy Efficiency and Renewable Energy, Office of Vehicle Technologies of the U.S. Department of Energy under Contract DE-AC02-05CH11231 under the Battery Materials Research Program. Funding for the electron microscopy work was provided by the Soft Matter Electron Microscopy Program (KC11BN), supported by the Office of Science, Office of Basic Energy Science, U.S. Department of Energy, under Contract No. DE- AC02-05CH11231. The electron microscopy work was performed at the Molecular Foundry. Didier Devaux was supported by a postdoctoral fellowship from the Philomathia Center at UC Berkeley. The microtomography experiments were carried out at the Advanced Light Source at Lawrence Berkeley National Laboratory at beamline 8.3.2. The Advanced Light Source and Molecular Foundry are supported by the Director, Office of Science, Office of Basic Energy Sciences, of the U. S. Department of Energy under Contract No. DE-AC02-05CH11231.

ORCID

Didier Devaux https://orcid.org/0000-0002-1964-0556
Irune Villaluenga https://orcid.org/0000-0002-1299-2479
Xi Jiang https://orcid.org/0000-0002-9589-7513
Yu Hao Chang https://orcid.org/0000-0003-4098-7287
Dilworth Y. Parkinson https://orcid.org/0000-0002-1817-0716
Nitash P. Balsara https://orcid.org/0000-0002-0106-5565

References

1. Z. Yang, J. Zhang, M. C. W. Kintner-Meyer, X. Lu, D. Choi, J. P. Lemmon, and J. Liu, "Electrochemical energy storage for green grid." *Chem. Rev.*, **111**, 3577 (2011).
2. J. B. Goodenough and K.-S. Park, "The Li-ion rechargeable battery: A perspective." *J. Am. Chem. Soc.*, **135**, 1167 (2013).
3. P. G. Bruce, S. A. Freunberger, L. J. Hardwick, and J.-M. Tarascon, "Li–O_2 and Li–S batteries with high energy storage." *Nat. Mater.*, **11**, 19 (2012).
4. N. P. Balsara and J. Newman, "Comparing the energy content of batteries, fuels, and materials." *J. Chem. Educ.*, **90**, 446 (2013).
5. M. Lécuyer, J. Gaubicher, M. Deschamps, B. Lestriez, T. Brousse, and D. Guyomard, "Structural changes of a Li/S rechargeable cell in lithium metal polymer technology." *J. Power Sources*, **241**, 249 (2013).
6. S. Waluś, C. Barchasz, R. Bouchet, J.-C. Leprêtre, J.-F. Colin, J.-F. Martin, E. Elkaïm, C. Baehtz, and F. Alloin, "Lithium/Sulfur batteries upon cycling: Structural modifications and species quantification by in situ and operando X-ray diffraction spectroscopy." *Adv. Energy Mater.*, **5**, 1500165 (2015).
7. S. S. Zhang, "Liquid electrolyte lithium/sulfur battery: Fundamental chemistry, problems, and solutions." *J. Power Sources*, **231**, 153 (2013).
8. K. H. Wujcik, D. R. Wang, A. A. Teran, E. Nasybulin, T. A. Pascal, D. Prendergast, and N. P. Balsara, "Determination of redox reaction mechanisms in lithium-sulfur batteries." *Electro. chemical. Engineering*, ed. R. C. Alkire, P. N. Bartlett, and M. T. Koper (John Wiley & Sons, Weinheim, Germany) p. 41 (2018).
9. H. S. Ryu, H. J. Ahn, K. W. Kim, J. H. Ahn, K. K. Cho, and T. H. Nam, "Self-discharge characteristics of lithium/sulfur batteries using TEGDME liquid electrolyte." *Electrochim. Acta*, **52**, 1563 (2006).
10. X. Ji, K. T. Lee, and L. F. Nazar, "A highly ordered nanostructured carbon–sulphur cathode for lithium–sulphur batteries." *Nat. Mater.*, **8**, 500 (2009).
11. X. Ji and L. F. Nazar, "Advances in Li–S batteries." *J. Mater. Chem.*, **20**, 9821 (2010).
12. G. Zheng, Y. Yang, J. J. Cha, S. S. Hong, and Y. Cui, "Hollow carbon nanofiber-encapsulated sulfur cathodes for high specific capacity rechargeable lithium batteries." *Nano Lett.*, **11**, 4462 (2011).
13. Y. Qiu et al., "High-rate, ultralong cycle-life lithium/sulfur batteries enabled by nitrogen-doped graphene." *Nano Lett.*, **14**, 4821 (2014).
14. Z. Li, J. Zhang, and X. W. Lou, "Hollow carbon nanofibers filled with MnO_2 nanosheets as efficient sulfur hosts for lithium–sulfur batteries." *Angew. Chemie Int. Ed.*, **54**, 12886 (2015).
15. X. Fan, W. Sun, F. Meng, A. Xing, and J. Liu, "Advanced chemical strategies for lithium–sulfur batteries: A review." *Green Energy Environ.*, **3**, 2 (2018).
16. G. He, S. Evers, X. Liang, M. Cuisinier, A. Garsuch, and L. F. Nazar, "Tailoring porosity in carbon nanospheres for lithium–sulfur battery cathodes." *ACS Nano*, **7**, 10920 (2013).
17. X.-B. Cheng, R. Zhang, C.-Z. Zhao, and Q. Zhang, "Toward safe lithium metal anode in rechargeable batteries: A review." *Chem. Rev.*, **117**, 10403 (2017).

18. M. Singh et al., "Effect of molecular weight on the mechanical and electrical properties of block copolymer electrolytes." *Macromolecules*, **40**, 4578 (2007).
19. A. Panday, S. Mullin, E. D. Gomez, N. Wanakule, V. L. Chen, A. Hexemer, J. Pople, and N. P. Balsara, "Effect of molecular weight and salt concentration on conductivity of block copolymer electrolytes." *Macromolecules*, **42**, 4632 (2009).
20. P. E. Trapa, B. Y. Huang, Y. Y. Won, D. R. Sadoway, and A. M. Mayes, "Block copolymer electrolytes synthesized by atom transfer radical polymerization for solid-state, thin-film lithium batteries." *Electrochem. Solid-State Lett.*, **5**, A85 (2002).
21. D. Devaux, D. Glé, T. N. T. Phan, D. Gigmes, E. Giroud, M. Deschamps, R. Denoyel, and R. Bouchet, "Optimization of block copolymer electrolytes for lithium metal batteries." *Chem. Mater.*, **27**, 4682 (2015).
22. T. A. Pascal, I. Villaluenga, K. H. Wujcik, D. Devaux, X. Jiang, D. R. Wang, N. Balsara, and D. Prendergast, "Liquid sulfur impregnation of microporous carbon accelerated by nanoscale interfacial effects." *Nano Lett.*, **17**, 2517 (2017).
23. P.-E. Dufils, N. Chagneux, D. Gigmes, T. Trimaille, S. R. A. Marque, D. Bertin, and P. Tordo, "Intermolecular radical addition of alkoxyamines onto olefins: An easy access to advanced macromolecular architectures precursors." *Polymer*, **48**, 5219 (2007).
24. M. Chintapalli, T. N. P. Le, N. R. Venkatesan, N. G. Mackay, A. A. Rojas, J. L. Thelen, X. C. Chen, D. Devaux, and N. P. Balsara, "Structure and ionic conductivity of polystyrene-block-poly(ethylene oxide) electrolytes in the high salt concentration limit." *Macromolecules*, **49**, 1770 (2016).
25. D. R. Wang et al., "Rate constants of electrochemical reactions in a lithium-sulfur cell determined by operando X-ray absorption spectroscopy." *J. Electrochem. Soc.*, **165**, A3487 (2018).
26. K. H. Wujcik et al., "Fingerprinting lithium-sulfur battery reaction products by X-ray absorption spectroscopy." *J. Electrochem. Soc.*, **161**, A1100 (2014).
27. D. R. Wang, K. H. Wujcik, A. A. Teran, and N. P. Balsara, "Conductivity of block copolymer electrolytes containing lithium polysulfides." *Macromolecules*, **48**, 4863 (2015).
28. K. J. Harry, D. T. Hallinan, D. Y. Parkinson, A. A. MacDowell, and N. P. Balsara, "Detection of subsurface structures underneath dendrites formed on cycled lithium metal electrodes." *Nat. Mater.*, **13**, 69 (2014).
29. D. Devaux, K. J. Harry, D. Y. Parkinson, R. Yuan, D. T. Hallinan, A. A. MacDowell, and N. P. Balsara, "Failure mode of lithium metal batteries with a block copolymer electrolyte analyzed by X-ray microtomography." *J. Electrochem. Soc.*, **162**, A1301–A1309 (2015).
30. A. A. MacDowell, D. Y. Parkinson, A. Haboub, E. Schaible, J. R. Nasiatka, C. A. Yee, J. R. Jameson, J. B. Ajo-Franklin, C. R. Brodersen, and A. J. McElrone, "X-ray micro-tomography at the Advanced Light Source." *Proc. SPIE*, **8506**, 850618 (2012).
31. D. T. Hallinan, S. A. Mullin, G. M. Stone, and N. P. Balsara, "Lithium metal stability in batteries with block copolymer electrolytes." *J. Electrochem. Soc.*, **160**, A464 (2013).
32. C. Barchasz, F. Molton, C. Duboc, J.-C. Leprêtre, S. Patoux, and F. Alloin, "Lithium/Sulfur cell discharge mechanism: An original approach for intermediate species identification." *Anal. Chem.*, **84**, 3973 (2012).
33. D.-W. Wang, Q. Zeng, G. Zhou, L. Yin, F. Li, H.-M. Cheng, I. R. Gentle, and G. Q. M. Lu, "Carbon–sulfur composites for Li–S batteries: status and prospects." *J. Mater. Chem. A*, **1**, 9382 (2013).
34. K. Kumaresan, Y. Mikhaylik, and R. E. White, "A mathematical model for a lithium–sulfur cell." *J. Electrochem. Soc.*, **155**, A576 (2008).
35. D. Devaux, X. Wang, J. L. Thelen, D. Y. Parkinson, J. Cabana, F. Wang, and N. P. Balsara, "Lithium metal-copper vanadium oxide battery with a block copolymer electrolyte." *J. Electrochem. Soc.*, **163**, A2447 (2016).
36. B. H. Toby and R. B. V. Dreele, "GSAS-II : The genesis of a modern open-source all purpose crystallography software package." *J. Appl. Crystallogr.*, **46**, 544 (2013).
37. L. Zielke et al., "Degradation of Li/S battery electrodes on 3D current collectors studied using X-ray phase contrast tomography." *Sci. Rep.*, **5**, 10921 (2015).